Journal of Materials Chemistry A

Accepted Manuscript

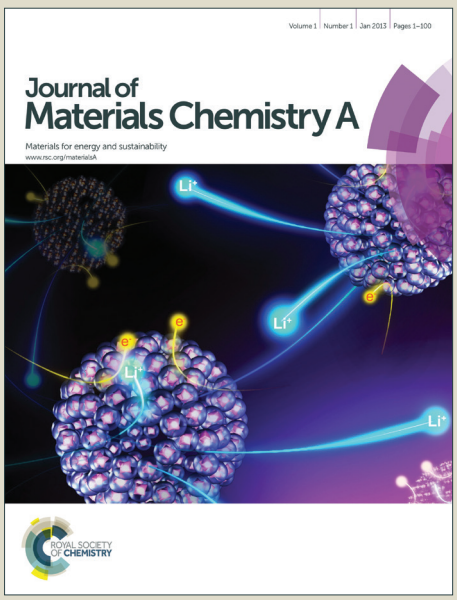

ROYAL SOCIETY OF CHEMISTRY

www.rsc.org/materialsA

Journal Name ARTICLE

Oxygen Vacancies in Self-Assemblies of Ceria Nanoparticles

Cite this: DOI: 10.1039/x0xx00000x

Mahasin Alam Sk,[a] Sergey M. Kozlov,[b] Kok Hwa Lim,*[ac] Annapaola Migani*[de] and Konstantin M. Neyman[bf]

Received ooth zzzzz 2014,
Accepted ooth xxxx 2014

DOI: 10.1039/x0xx00000x

www.rsc.org/

Cerium dioxide (CeO_2, ceria) nanoparticles possess size-dependent chemical properties, which may be very different from those of the bulk material. Agglomeration of such particles in nanoarchitectures may further significantly affect their properties. We computationally model the self-assembly of Ce_nO_{2n} particles (n = 38, 40, 80) – zero-dimensional (0D) structures – in one- and two-dimensional (1D and 2D) nanoarchitectures employing density-functional methods. The electronic properties of 1D $Ce_{80}O_{160}$ and 2D $Ce_{40}O_{80}$ resemble those of larger 0D crystallites, $Ce_{140}O_{280}$, rather than those of their building blocks. These 0D, 1D and 2D nanostructures are employed to study the size dependence of the formation energy of oxygen vacancy, $E_f(O_{vac})$, a central property in ceria chemistry. We rationalize within a common electronic structure framework the variations of the $E_f(O_{vac})$ values, which are computed for the Ce_nO_{2n} nanostructures with different size and dimensionality. We identify: i) the bandwidth of the unoccupied density of states projected onto the Ce 4f levels as an important factor, which controls $E_f(O_{vac})$; and ii) the corner Ce atoms as the structural motif essential for a noticeable reduction of $E_f(O_{vac})$. These results help to understand the size dependent behaviour of $E_f(O_{vac})$ in nanostructured ceria.

Introduction

Cerium dioxide (ceria) is an indispensable component of a broad variety of materials for industrial applications, ranging from oxygen sensors and permeation membranes to bio- and medical materials.[1] Usage of ceria in catalysis alone represents a very rapidly growing area with a huge market.[2] Remarkably, some properties of ceria change considerably when the size of its crystallites is decreased to nanoscale.[1,3] For example, ceria nanoparticles (NPs) of ~3-4 nm were shown to improve the catalytic performance of supported gold species by orders of magnitude compared to the situation when the support is less dispersed.[4,5] These experimental observations were rationalized by means of calculations based on density-functional theory (DFT), which showed that the formation of oxygen vacancy (O_{vac}) is greatly facilitated in ceria NPs[6,7] with respect to the bulk material.[8]

A combined DFT and synchrotron-radiation photoelectron spectroscopy study showed oxygen spillover to Pt species deposited on ceria to require the presence of nanostructured ceria.[9] This indicates that oxygen transfer through the ceria–Pt boundary is a nanoscale effect, and that nanostructured ceria is crucial to form key catalytic sites such as Pt-O.[10] Very recently it was shown that nanostructured ceria leads to a remarkable stabilization of platinum deposited in atomically dispersed form. This finding enables to maximize usage of this precious metal in catalytic materials.[11]

Strong size- and shape-dependence of the properties of the ceria nanostructures boosted intense experimental efforts, which resulted in the preparation of various ceria nanopolyhedra (truncated octahedra, cubes, etc.).[12,13] Zero-dimensional (0D) ceria nanopolyhedra can form structures extended in one (1D, e.g. nanowires, rods and tubes) and two dimensions (2D, e.g. nanogrids), either by self-assembly[13,14] or in the course of direct synthesis.[12,15] These 1D and 2D nanoarchitectures expose not only the most stable (111) planes of ceria but also more reactive (100) and (110) planes. Thus, the reactivity of nanoscale ceria can be tuned in a controllable fashion.1

Recent atomistic simulations using interatomic potentials explored the strain and architecture-tuned reactivity of ceria nanostructures to oxidize CO to CO_2.[16] These studies revealed that the tension is an activating factor, whereas the compression hinders the reaction. To the best of our knowledge, no results of DFT-based studies of 1D or 2D nanostructures formed via the self-assembly of ceria NPs have been published yet.

Herein, we computationally model the directional[17,18] self-assembly of Ce_nO_{2n} particles (n = 38, 40, 80) in 1D and 2D nanoarchitectures employing density-functional methods. We use the Perdew-Wang91[19-21] functional augmented with a Hubbard-type term U = 4 eV[22] for the Ce 4f electrons (PW91+4 approximation).[23,24] We address the formation of the most stable single oxygen vacancy in the Ce_nO_{2n} particles and their self-assemblies, focusing on the dependence of the formation energy of oxygen vacancy, $E_f(O_{vac})$, on the size and dimensionality. To this end, the $E_f(O_{vac})$ values of the 1D and 2D structures are compared to those of their respective building blocks. Moreover, the electronic properties and the $E_f(O_{vac})$ values of the Ce_nO_{2n} particles ($n \leq 80$) and their nanoarchitectures are compared to those of a ~2.4 nm large $Ce_{140}O_{280}$ nanocrystallite.[25]

Finally, we address the reliability of the trends derived for $E_f(O_{vac})$ in ceria nanostructures from contemporary electronic structure calculations. For this purpose, we evaluate $E_f(O_{vac})$ for ceria nanostructures with 40 CeO_2 units, including the previously reported $Ce_{40}O_{80}$´ model,[6,7] with the HSE06 variant of the Heyd–Scuseria–Ernzerhof hybrid functional.[26-29] These values are used in conjunction with the HSE06 $E_f(O_{vac})$ values computed for suitably small regular[30,31] and vicinal stepped[31] $CeO_2(111)$ surface models and the $Ce_{21}O_{42}$[6,7] model to derive general oxygen mobility trends in ceria.

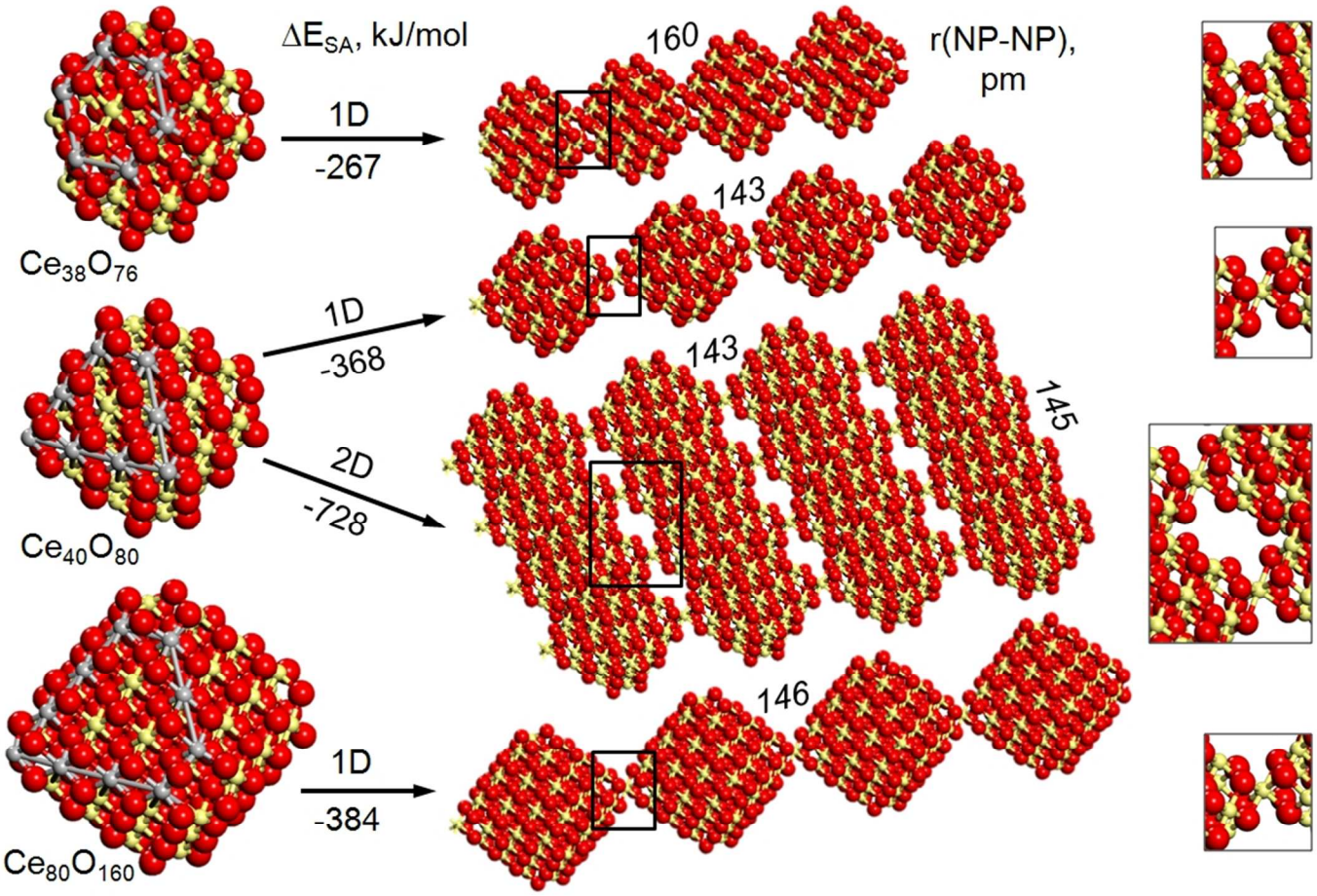

Fig. 1 Sketches of stoichiometric ceria NPs Ce_nO_{2n}, n = 38, 40, 80, and their self-assemblies generated via the binding of the four O atoms of the {100} facet to four corner Ce atoms (n = 38) or one corner Ce atom (n = 40, 80), as detailed in the insets. Ce^{4+} cations – light beige spheres, O^{2-} anions – red spheres, edges of one {111} facet – grey spheres. The ΔE_{SA} [kJ/mol] values are the PW91+4 self-assembly energies; the r(NP-NP) [pm] values are the optimized heights of the corner Ce atoms over the O_4 planes.

Computational methods

Periodic DFT calculations were carried out using the VASP[32,33] package and employing the Perdew-Wang[19-21] (PW91) implementation of the generalized gradient approximation (GGA) for the exchange-correlation functional. An effective on-site Coulomb correction U_{eff} = 4 eV[22] was applied to the Ce 4f levels within the GGA+U scheme[23,24](referred to as PW91+4). The computationally very demanding hybrid exchange correlation functional by Heyd–Scuseria–Ernzerhof (HSE),[26,27] previously tested for partially reduced CeO_2(111) surfaces[8,34] and (in a slightly modified form) for Ce_2O_3 bulk[35] was also used to obtain alternative supposedly more accurate8 comparative $E_f(O_{vac})$ estimates. The HSE functional was used with the screening parameter of 2 nm^{-1} corresponding to the HSE06 scheme. Following the procedure adopted in refs. 6 and 7, HSE06 single-point energy calculations were carried out at the PW91+4 optimized pristine and oxygen atom defective geometries. Importantly, the position of the Ce^{3+} pair of atoms of the oxygen defective geometries is the same in the corresponding PW91+4 and HSE06 calculations. This procedure is expected to reproduce O activity trends derived from computationally exceedingly expensive HSE06 optimizations although some numerical differences may exist.

A plane-wave basis with a 415 eV cut-off for the kinetic energy and projector–augmented wave[36] description of core-valence electron interactions were employed. The calculations were done at the Γ–point. Single-point total energy convergence tolerance at the self-consistency was set to 10^{-6} eV. The structures were optimized until a maximum force less than 2 eV/pm was obtained.

In the spin-polarized calculations of the oxygen atom defective nanostructures, the ferromagnetic alignment of the two localized Ce 4f electrons resulting in a total magnetic moment $\mu = 2\mu_B$ was assumed. For the regular and vicinal CeO_2(111) surface models an antiferromagnetic alignment of the two localized Ce 4f electrons resulting in a total magnetic moment $\mu = 0\mu_B$ was sometimes obtained. The charge of the O and Ce atoms forming the Ce-O_4 and Ce_4-O_4 contacts between NPs was characterized by topological Bader analysis.[37] The $E_f(O_{vac})$ energies are calculated from the total energies of the stoichiometric and O defective systems with respect to ½ of the O_2 molecule triplet state energy, $E(O_2)$ = -9.82 (-17.03) eV with PW91+4 (HSE06).

A unit cell of 2.5 nm × 2.5 nm × 2.5 nm was used for the 0D $Ce_{40}O_{80}$ building block. 0D $Ce_{40}O_{80}$ (Fig. 1) has two equatorial Ce corner atoms, which can interact with the O_4 unit located at the axial position in the x- and y-direction, upon decreasing the *a* and *b* cell parameters, respectively. The 1D $Ce_{40}O_{80}$ structure was constructed by gradually decreasing the

cell parameter *a*, and optimizing the atomic positions. The lowest energy was obtained in this procedure for a unit cell of 1.612 nm × 2.5 nm × 2.5 nm, which identifies the optimized geometry for the 1D $Ce_{40}O_{80}$ nanowire. Starting from the 1.612 nm × 2.5 nm × 2.5 nm unit cell of 1D $Ce_{40}O_{80}$, a similar procedure was repeated to construct the 2D $Ce_{40}O_{80}$ nanogrid, by repeatedly shrinking the cell parameter *b*, and optimizing the atomic positions. The lowest energy was obtained for a unit cell of 1.612 nm × 1.607 nm × 2.5 nm, which corresponds to the 2D $Ce_{40}O_{80}$ optimized geometry.

Similarly, the 0D $Ce_{80}O_{160}$ building block has one Ce corner atom (Fig. 1), which can interact with the O_4 unit located at the axial position in the self-assembling x-direction. The unit cell for the 0D $Ce_{80}O_{160}$ building block is 3 nm × 2.5 nm × 2.5 nm, and for the optimized 1D $Ce_{80}O_{160}$ nanostructure is 2.145 nm × 2.5 nm × 2.5 nm. The unit cell for the 0D $Ce_{38}O_{76}$ nanostructure is 2.2 nm × 2.5 nm × 2.5 nm, and for the optimized 1D $Ce_{38}O_{76}$ nanowire is 1.303 nm × 2.5 nm × 2.5 nm. The unit cell for the $Ce_{140}O_{280}$ NP is 2.487 nm × 2.487 nm × 2.902 nm. The cells employed ensure an inter-particle distance ≥ 1 nm in each direction for the building blocks and in each not connected direction for the 1D and 2D nanoarchitectures, and an inter-particle distance ≥ 0.6 nm in each direction for $Ce_{140}O_{280}$.

The average energy of the 4f levels, ε_{4f}, corresponds to the first moment of the density of states projected (PDOS) onto the Ce 4f levels, $\rho_{4f}(\varepsilon)$, i.e., $\varepsilon_{4f} = \frac{\int_{\varepsilon_{Fermi}}^{+\infty} \varepsilon \cdot \rho_{4f}(\varepsilon) d\varepsilon}{\int_{\varepsilon_{Fermi}}^{+\infty} \rho_{4f}(\varepsilon) d\varepsilon}$. The average energy of the 4f levels of the Ce atom *i* (*i = corner 1, corner 2, edge, facet)*, ε_{4f}^{i}, corresponds to the first moment of the corresponding PDOS. The ε_{4f}, and ε_{4f}^{i} values are shifted with respect to the vacuum level, ε_{vacuum}, to enable comparison between different structures. The bandwidth of the 4f levels, W_{4f}, is estimated as the full width at half maximum of a Gaussian distribution with standard deviation equals to the square root of the Ce 4f PDOS variance, σ_{4f}, i.e., $W_{4f} \sim 2\sqrt{2 \ln 2}\, \sigma_{4f}$ where $\sigma_{4f} = \sqrt{\frac{\int_{\varepsilon_{Fermi}}^{+\infty} (\varepsilon - \varepsilon_{4f})^2 \cdot \rho_{4f}(\varepsilon) d\varepsilon}{\int_{\varepsilon_{Fermi}}^{+\infty} \rho_{4f}(\varepsilon) d\varepsilon}}$. ε_{4f} and W_{4f} are analogous[38] to the *d* band center and *d* band width commonly used as descriptors for bulk and surface systems.

The convergence with respect to the k-point density was examined for 2D $Ce_{40}O_{80}$ with a Monkhorst-Pack 3 × 3 × 1 k-point mesh. This calculation gives ε_{4f} and $\varepsilon_{4f}^{corner\ 1}$ values identical within the given accuracy to the Γ−point calculation values, and a total energy within 0.02 eV with respect to the Γ−point calculation energy. The convergence with respect to the vacuum thickness was checked for the $Ce_{40}O_{80}'$ particle (Fig. S1). The ε_{4f} = -3.67 eV and $\varepsilon_{4f}^{corner\ 1}$ = -3.80 eV values in Table 1 are obtained from a calculation, which employed a 2.2 nm × 1.9 nm × 1.9 nm cell (inter-particle separation ≥ 0.6 nm).[6,7] Similar results (ε_{4f} = -3.69 eV and $\varepsilon_{4f}^{corner\ 1}$ = -3.82) are obtained from a calculation, which employs a 2.5 nm × 2.5 nm × 2.5 nm cell (inter-particle separation ≥ 1 nm).

The regular CeO_2(111) surface and the vicinal surfaces with type I, II, and III steps were modelled by three O-Ce-O tri-layer thick slabs.[31] To model CeO_2(111), we used a hexagonal *p*(3×3) unit cell of 1.150 nm × 1.150 nm × 1.935 nm. For type I, II, and III steps, we employed the 0.763 nm × 1.479 nm × 3 nm (α = 102.17º, β=90.00º, γ= 82.58º), 0.763 nm × 1.266 nm × 3 nm (α=75.74º, β=90.00º, γ=81.33º), and 0.661 nm × 1.376 nm × 3 nm (α=76.95º, β=90.00º, γ=94.59º) unit cells, respectively. These unit cells were constructed using the experimental lattice constant for CeO_2 bulk, 541 pm,[39,40] and ensuring a vacuum layer thickness ≥ 1 nm. During the geometry optimization all three O-Ce-O tri-layers were relaxed for the stepped surfaces, while only the top two O-Ce-O tri-layers were relaxed for the regular surface. Type I and II unit cells have composition 3 × Ce_8O_{16}, and type III unit cell has composition 3 × Ce_7O_{14}.

Results and discussion

Self-assembly of ceria nanoparticles in 1D and 2D structures.

Experiments show that NPs with diameter ∅ ~ 3÷10 nm commonly have truncated octahedral morphologies enclosed by extended {111} facets and small (up to four atom column width)[41] {100} facets.[42] The morphology emerging from the simulations based on interatomic potentials is in full accord with the experiment.[25,43] The truncated octahedral Ce_nO_{2n} (n= 38, 40, 80 and 140) models in the ~ 1.5÷2.4 nm size range generated by global optimization[25] all have apical {100} facets made of four oxygen atoms, O_4 site. Compared with the bulk octahedral cuts,[44,45] the Ce_nO_{2n} (n= 40, 80 and 140) models have an increasing number of missing Ce atoms (four, five and six, respectively) at the vertices of the octahedra.

Here the $Ce_{40}O_{80}$ (∅ ~ 1.5 nm) and $Ce_{80}O_{160}$ (∅ ~ 1.9 nm) NPs are used as building blocks for the self-assembly of higher-order 1D and 2D nanoarchitectures through a corner-to-facet interaction (Fig. 1). The $Ce_{80}O_{160}$ building block has one corner Ce atom and an O_4 site directly across from each other. A regular 1D $Ce_{80}O_{160}$ wire is formed through the binding of the corner Ce atom of a NP with the O_4 site of another NP with similar orientation, i.e., Ce-O_4 binding.

The $Ce_{40}O_{80}$ and $Ce_{40}O_{80}'$ NPs are structural isomers with truncated octahedral shape (Fig. S1). $Ce_{40}O_{80}$ is 55 kJ/mol higher in energy (Table 1) than $Ce_{40}O_{80}'$. In $Ce_{40}O_{80}'$ the two corner Ce atoms are directly across from each other. In this arrangement they cannot be used to connect NPs with similar orientation. In the $Ce_{40}O_{80}$ NP the two corner Ce atoms are directly across from O_4 sites. In this case, the NP can interact with another similarly oriented NP in one or two directions via Ce-O_4 binding. The binding in one direction leads to the formation of the 1D $Ce_{40}O_{80}$ wire and the concurrent Ce-O_4 binding in the two orthogonal directions leads to the creation of the 2D $Ce_{40}O_{80}$ grid.

Among the truncated octahedral structures, the somewhat smaller (∅ ~ 1.1 nm) $Ce_{38}O_{76}$ particle is also interesting as it can be used as building block to form a 1D wire through a facet-to-facet binding mechanism (Fig. 1). The $Ce_{38}O_{76}$ NP corresponds to a sub-system of the $Ce_{40}O_{80}$ NP.[46] When $Ce_{40}O_{80}$ is reduced in size by removing a CeO_4 unit from one corner and an additional Ce corner atom to maintain the stoichiometry, a {100} facet with four four-coordinated Ce atoms is formed. These open Ce sites can interact with the four O atoms of a {100} facet of another similarly oriented $Ce_{38}O_{76}$ NP to form a 1D wire, i.e., Ce_4-O_4 binding.

The energy gained in the self-assembly, ΔE_{SA}, of the Ce_nO_{2n} (n = 38, 40, 80) building blocks is reported in Fig. 1. The "reaction" coordinate is given by the inter-particle separation, r(NP-NP), measured as the height of the corner Ce atom over the O_4 plane of the Ce-O_4 or Ce_4-O_4 contact formed between contiguous NPs. The self-assembled structure corresponds to the energy minimum in the interacting particle energy profile along the r(NP-NP) reaction coordinate at 160, and 143-146 pm (Fig. 1) for the facet-to-facet and corner-to-facet self-assembly, respectively. The self-assembly energy profile has no barrier and

Table 1. Calculated PW91+4 data for the 0D, 1D and 2D Ce_nO_{2n} nanostructures: excess energy per CeO_2 unit with respect to the energy of ceria bulk (ΔE), average energy of the 4f levels of the connecting corner Ce atom 1, ($\varepsilon_{4f}^{corner\,1}$), average energy of the 4f levels of the connecting corner Ce atom 2, ($\varepsilon_{4f}^{corner\,2}$), average energy of the total 4f levels, (ε_{4f}), bandwidth of the PDOS on the 4f levels, (W_{4f}), energy of the highest energy peak of the PDOS on the 2p levels of the O_4 site, from which the O_{2c} atom is removed upon vacancy formation, ($\varepsilon_{2p}^{O_{2c}}$), O 2p HOMO and Ce 4f LUMO energy difference, (Δε), lowest O_{2c} vacancy formation energy, ($E_f(O_{vac})$). The $\varepsilon_{4f}^{corner\,1}$, $\varepsilon_{4f}^{corner\,2}$, ε_{4f} and $\varepsilon_{2p}^{O_{2c}}$ values are with respect to the vacuum level, ε_{vacuum}.

Building block	System	ΔE, kJ/mol	$\varepsilon_{4f}^{corner\,1}$, eV	$\varepsilon_{4f}^{corner\,2}$, eV	ε_{4f}, eV	W_{4f}, eV	$\varepsilon_{2p}^{O_{2c}}$, eV	$\Delta\varepsilon$, eV	$E_f(O_{vac})$, kJ/mol
$Ce_{38}O_{76}$[a]	0D	121.9	-4.21	-	-3.89	0.82	-5.67	0.74	5
	1D	114.9	-4.10	-	-4.03	0.38	-6.05	1.52	149
$Ce_{40}O_{80}$´	0D	107.8	-3.80	-3.80	-3.67	0.35	-5.55	1.49	77[b]
$Ce_{40}O_{80}$	0D[c]	109.2	-3.97	-3.97	-3.85	0.54	-5.55	0.97	39
	1D	100.0	-3.68	-4.05	-3.84	0.49	-5.68	1.15	57
	2D	91.0	-3.85	-3.85	-3.86	0.24	-5.83	1.76	157
$Ce_{80}O_{160}$	0D	81.1	-4.24	-	-3.87	0.54	-5.60	0.98	45[b]
	1D	76.3	-3.89	-	-3.87	0.26	-5.71	1.63	103
$Ce_{140}O_{280}$	0D	64.5	-	-	-3.83	0.26	-5.68	1.63	145

[a]See Ref. 25 for the global minimum structure. [b]Refs. 6, 7. [c]See text for description on how the building block has been designed by rearrangement of the $Ce_{40}O_{80}$´ model (Fig. S1).

decreases slowly in a first stage (r(NP-NP) ~ 0.6 nm) as the building blocks approach each-other, and rapidly afterwards until the energy minimum. A similar energy profile was found based on DFT calculations for 1D Pd_n nanowires constructed from isolated cuboctahedral Pd_n (n=38, 79, 140, 225) species.[18]

ΔE_{SA} depends only weakly on the size of the building blocks but depends noticeably on the type of connector. Despite the size difference, the self-assembly energies computed for the 1D $Ce_{40}O_{80}$ and $Ce_{80}O_{160}$ nanowires (-368 and -384 kJ/mol per Ce-O_4 corner-to-facet contact, respectively) are close to each other. This indicates that for the Ce-O_4 corner-to-facet interaction ΔE_{SA} is converged with respect to the size of the Ce_nO_{2n} building block within ≤ 20 kJ/mol for n ≥40. This size agrees with the size required to obtain adsorption energies for weakly interacting probe molecules (i.e., CO) on Ce_nO_{2n} NPs converged with respect to the NP size.

The geometry difference in the $Ce_{40}O_{80}$ template, which has an additional corner Ce atom compared to the $Ce_{80}O_{160}$ NP, seems not to significantly change ΔE_{SA} for 1D $Ce_{40}O_{80}$ vs. 1D $Ce_{80}O_{160}$. Likewise, the energy gained in the creation of the second Ce-O_4 corner-to-facet contact in 2D $Ce_{40}O_{80}$ (-360 kJ/mol) is almost the same as the energy gained in the creation of the first Ce-O_4 contact. These all are indications of a rather local character of the inter-particle interaction, which is hardly affected by more distant atoms of the NP.

On the other hand, ΔE_{SA} for $Ce_{38}O_{76}$ is notably smaller (-267 kJ/mol) despite the small difference in size with $Ce_{40}O_{80}$. This lower energy gain is attributable to the longer Ce-O bonds between the Ce and O atoms in the Ce_4-O_4 contact as compared to the Ce-O_4 contact. In 1D $Ce_{38}O_{76}$ the contact is provided by an O_4 unit, which is bound to two equivalent Ce_4 units on opposite sides. In this configuration, the O atoms are four-coordinated and have four equivalent Ce-O bond lengths (251 pm), while the Ce atoms are six-coordinated. The Ce atom of the Ce-O_4 contact is equivalently bound to two O_4 units, and therefore is eight-coordinated with eight equivalent Ce-O 243 pm long bonds.

A Bader charge analysis[37] shows that the driving force for the self-assembly principally originates from electrostatic factors. The positive charge of the corner Ce atom changes upon formation of the Ce-O_4 contact from the value of a four-coordinated corner Ce atom (2.14|e|) to a typical charge value of a bulk eight-coordinated Ce atom (2.37|e|) in the Ce-O_4 contact. This is compensated by an increment of negative charge (from -1.09|e| to -1.15|e|) of each of the four O atoms involved in the corner-to-facet interaction. In the facet-to-facet binding, there is an increment of the negative change by 0.12|e| per O atom (from -1.10|e| to -1.22|e|) for the O atoms of the Ce_4-O_4 contact. This is counterbalanced by an increment of the positive charge (from 2.16|e| to 2.23|e|) per Ce atom for the two Ce_4 units on opposite sides of the O_4 unit. The smaller increment of the positive charge per Ce atom in the Ce_4-O_4 contact as compared to the Ce-O_4 contact reflects the smaller coordination number of the Ce atoms in Ce_4-O_4 contact (six) as compared to the Ce-O_4 contact (eight). Similarly, the larger increment of negative charge per O atom in the Ce_4-O_4 contact as compared to the Ce-O_4 contact is due to the larger coordination number of the O atoms in the Ce_4-O_4 contact (four) as compared to the Ce-O_4 contact (three).

The structural changes induced by the formation of the contacts between the NPs are local and involve a minority of atoms. Nevertheless they have a noticeable impact on the global electronic structure of the nanoarrays. In order to understand this effect, in Fig. 2 we report the occupied total DOS, and the unoccupied PDOS on the total 4f levels, which essentially coincides with the unoccupied total DOS in this energy range, for the Ce_nO_{2n} (n=38, 40, 80) NPs, their 1D and 2D self-assemblies, $Ce_{40}O_{80}$´ and $Ce_{140}O_{280}$.[48] Moreover, we consider the unoccupied PDOS on the 4f levels of one corner Ce atom, and the occupied PDOS on the 2p levels of the binding O_4 site for all structures except $Ce_{40}O_{80}$´ and $Ce_{140}O_{280}$. Note that it is sufficient to analyse only one of the Ce corner atoms because of symmetry. We use different colors to differentiate the PDOS of the free (blue) and connected (green) corner Ce atom and O_4 site. The vertical blue (green) line indicates the average energy of

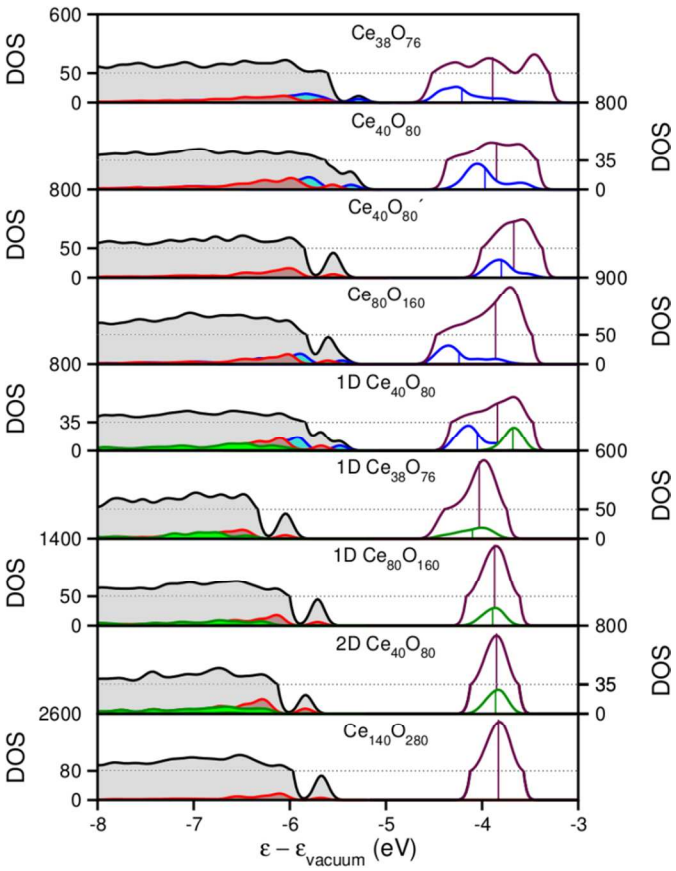

Fig. 2 Occupied total DOS (black) and PDOS on the 2p levels of the O_4 site from which the O_{2c} atom is removed upon vacancy formation (red), and unoccupied PDOS on the total 4f levels of the Ce atoms (violet). Occupied PDOS on the 2p levels of the binding O_4 site and unoccupied PDOS on the 4f levels of one corner Ce atom for the free (blue) and connected (green) atoms. DOS and PDOS units are number of states eV^{-1} $cell^{-1}$. The vertical lines indicate the average energy of the unoccupied 4f levels of all Ce atoms (violet), and free (blue) and connected (green) corner Ce atoms (see Table 1). Energies are with respect to the vacuum level, ε_{vacuum}. Filling denotes occupied levels. The dotted line indicates the separation between the two different scales in the vertical axis used to plot the black DOS and violet PDOS.

the 4f levels of the free (connected) corner Ce atom, $\varepsilon_{4f}^{corner\,1}$ and $\varepsilon_{4f}^{corner\,2}$. We consider the shift of $\varepsilon_{4f}^{corner\,1}$ and $\varepsilon_{4f}^{corner\,2}$ with respect to the average energy of the total Ce 4f levels, ε_{4f} (vertical violet line), and the bandwidth of the PDOS on the Ce 4f levels, as measured by W_{4f} (Table 1).

Based on Fig. 2 and Table 1, we can assess the convergence of the electronic properties of the Ce_nO_{2n} (n=38, 40, 80) NPs, and their 1D, and 2D assemblies as function of the size and dimensionality. First of all, W_{4f} decreases across the series $Ce_{38}O_{76}$ > $Ce_{40}O_{80}$, 1D $Ce_{40}O_{80}$, $Ce_{80}O_{160}$ > $Ce_{40}O_{80}$´, 1D $Ce_{38}O_{76}$ > 1D $Ce_{80}O_{160}$, $Ce_{140}O_{280}$, 2D $Ce_{40}O_{80}$. This trend correlates with the number and type of corner Ce atoms. W_{4f} is the largest for the $Ce_{38}O_{76}$ NP with four corner Ce atoms, which are placed at the intersection between a Ce-terminated {100} facet and {111} facets. W_{4f} is the smallest for the structures with no corner Ce atoms ($Ce_{140}O_{280}$) or for the structures whose corner Ce atoms have completed their oxygen coordination sphere via the formation of the Ce-O_4 contacts (1D $Ce_{80}O_{160}$, 2D $Ce_{40}O_{80}$). Finally W_{4f} is intermediate for the structures, which have two ($Ce_{40}O_{80}$) or one (1D $Ce_{40}O_{80}$, $Ce_{80}O_{160}$) free corner Ce atoms of intersecting {111} facets.

At the same time ε_{4f} is essentially constant across the series, with the exception of 1D $Ce_{38}O_{76}$ (slightly stabilized by ca. 0.1 eV) and $Ce_{40}O_{80}$´ (slightly destabilized by ca. 0.1 eV). $\varepsilon_{4f}^{corner\,1}$ and $\varepsilon_{4f}^{corner\,2}$ for $Ce_{40}O_{80}$ and $Ce_{40}O_{80}$´, $\varepsilon_{4f}^{corner\,1}$ for $Ce_{38}O_{76}$ and $Ce_{80}O_{160}$, and $\varepsilon_{4f}^{corner\,2}$ for 1D $Ce_{40}O_{80}$ (vertical blue lines in Fig. 2) are noticeably downshifted with respect to ε_{4f}. On the other hand $\varepsilon_{4f}^{corner\,1}$ for 1D $Ce_{80}O_{160}$, and $\varepsilon_{4f}^{corner\,1}$and $\varepsilon_{4f}^{corner\,2}$ for 2D $Ce_{40}O_{80}$ (vertical green lines in Fig. 2) coincide with ε_{4f}. $\varepsilon_{4f}^{corner\,1}$ for 1D $Ce_{38}O_{76}$ is slightly downshifted (ca. 0.1 eV) with respect to ε_{4f}.

Moreover, the shape of the PDOS on the 4f levels of the free and connected corner Ce atoms is different: it corresponds to a symmetric Gaussian distribution for the connected corner Ce atoms while it is rather distorted with respect to a Gaussian distribution for the free corner Ce atoms. This indicates that it is the free Ce corner atoms, which cause the deformation of the PDOS on the total 4f levels with respect to a symmetric Gaussian distribution as shown in Fig. 2.

The properties of the 4f levels for 1D $Ce_{38}O_{76}$ are different from those computed for 1D $Ce_{80}O_{160}$, 2D $Ce_{40}O_{80}$ and $Ce_{140}O_{280}$. This difference is related to the structure of the Ce_4-O_4 contact previously discussed, whose Ce-O bonds (251 pm) are elongated with respect to the average Ce-O bond length between six-coordinated Ce atoms and four-coordinated O atoms (230 pm) found in $Ce_{140}O_{280}$. As a result W_{4f} is larger and ε_{4f} is slightly red-shifted as compared to 1D $Ce_{80}O_{160}$, 2D $Ce_{40}O_{80}$ and $Ce_{140}O_{280}$. This shows that even local geometric effects appreciably influence the global electronic structure.

The formation of the Ce-O_4 and Ce_4-O_4 contacts has an opposite effect on the 2p levels of the O atoms of the contacts, which are shifted to lower energies after the contact is formed (Fig. 2).

The 1D, and 2D nanoarrays depicted in Fig. 1 have additional O_4 sites at {100} facets, which are not involved in the Ce-O_4 or Ce_4-O_4 contacts, with two-coordinated oxygen atoms, O_{2c}. In Fig. 2 we report the occupied PDOS on the 2p levels of one of the equivalent O_4 sites, which do not form contacts, for the nanoarrays and their building blocks, and the occupied PDOS on the 2p levels of one of the equivalent O_4 sites for $Ce_{40}O_{80}$´and $Ce_{140}O_{280}$. In particular we focus on the energy of the highest energy peak of the PDOS, $\varepsilon_{2p}^{O_{2c}}$, which is an important descriptor for the behavior of $E_f(O_{vac})$ for creation of an O_{2c} vacancy at these O_4 sites. We find that $\varepsilon_{2p}^{O_{2c}}$ is stabilized by 0.11-0.13 eV upon formation of one Ce-O_4 contact (1D Ce_nO_{2n} (n=40, 80) versus their respective building blocks) and by twice as much (0.28 eV) upon formation of two Ce-O_4 contacts (2D $Ce_{40}O_{80}$ with respect to $Ce_{40}O_{80}$). In the case of the Ce_4-O_4 contact the $\varepsilon_{2p}^{O_{2c}}$ stabilization is even larger (0.38 eV), as eight new Ce-O bonds (two per O atom) are formed (Table 1).

Fig. 2 indicates that the electronic structure of 1D $Ce_{80}O_{160}$ and 2D $Ce_{40}O_{80}$ resembles more that of a $Ce_{140}O_{280}$ rather than that of their respective 0D building blocks. A shift of $\varepsilon_{2p}^{O_{2c}}$ towards lower energies and a decrease of W_{4f}, with increasing the dimensionality is found for 0D, 1D and 2D $Ce_{40}O_{80}$. Overall, this shows that the self-assembly of the Ce_nO_{2n} building blocks in 1D and 2D structures effectively corresponds to increasing the size of the building block.

Formation of oxygen vacancies in ceria nanoarchitectures.

The O_4 sites, which do not take part in the Ce-O_4 or Ce_4-O_4 contacts, have been probed for their ability to release O_{2c} atoms (Fig. 3). The removal of such O_{2c} atoms was reported to require the least $E_f(O_{vac})$ in the $Ce_{21}O_{42}$, $Ce_{40}O_{80}$´ and $Ce_{80}O_{160}$ NPs in comparison with the facet, sub-facet and interior O atoms.[6,7] Depending on the configuration of the Ce^{3+} ions, formed upon O atom removal, $E_f(O_{vac})$ for a given NP size varies within a few tenths of an electronvolt.[6,7] The

energetically most stable Ce^{3+} configuration is obtained upon localization of the two 4f excess electrons at corner or edge Ce atoms.[6,7] The computed most stable Ce^{3+} configurations are shown in Fig. 3 (see Fig. S2 for other low-energy Ce^{3+} configurations).

Previously[6,7] we showed that $E_f(O_{vac})$ is controlled by the energy separation between the occupied 2p levels of the O_{2c} atom, which is removed, and the unoccupied 4f levels of the Ce atoms, which receive the two excess electrons of the removed O_{2c} atom in the pristine systems. Accordingly, the $E_f(O_{vac})$ trends are discussed in terms of the $\varepsilon_{2p}^{O_{2c}}$ energies of the removed O_{2c} atoms and the average energies of the 4f levels of the Ce^{4+} cations, which become reduced upon O_{2c} atom removal, ε_{4f}^{site}, in the pristine stoichiometric structure. Larger W_{4f} values, i.e., $\varepsilon_{4f}^{site} < \varepsilon_{4f}$, imply smaller $E_f(O_{vac})$ values. Concomitantly, lower $\varepsilon_{2p}^{O_{2c}}$ values imply larger $E_f(O_{vac})$.

In the $Ce_{40}O_{79}$ structure the two 4f excess electrons were localized separately at the two free corner Ce sites ($\varepsilon_{4f}^{corner\,1} = \varepsilon_{4f}^{corner\,2}$ = -3.97 eV in pristine $Ce_{40}O_{80}$). The 1D $Ce_{40}O_{80}$ structure has one connected corner Ce atom ($\varepsilon_{4f}^{corner\,1}$ = -3.68 eV) and one free corner Ce atom ($\varepsilon_{4f}^{corner\,2}$ = -4.05 eV). Therefore, in 1D $Ce_{40}O_{79}$ one 4f electron was localized at the free corner Ce atom, and the other 4f electron was localized at a nearby edge Ce site (ε_{4f}^{edge} = -4.05 eV, in 1D $Ce_{40}O_{80}$). The computed lowest-energy configuration for 2D $Ce_{40}O_{79}$ has both the Ce^{3+} cations at equivalent edge sites, (ε_{4f}^{edge} = -3.88 eV in 2D $Ce_{40}O_{80}$). The $E_f(O_{vac})$ trend computed as a function of the dimensionality for these Ce^{3+} configurations, $Ce_{40}O_{80}$ ≤ 1D $Ce_{40}O_{80}$ << 2D $Ce_{40}O_{80}$, is directly related to the $\varepsilon_{2p}^{O_{2c}}$ and W_{4f} values in these structures (Table 1). 2D $Ce_{40}O_{80}$ with the lowest $\varepsilon_{2p}^{O_{2c}}$, the smallest W_{4f}, and a well-shaped Gaussian 4f PDOS, has the highest $E_f(O_{vac})$ value (157 kJ/mol) among the 0D, 1D and 2D $Ce_{40}O_{80}$ structures.

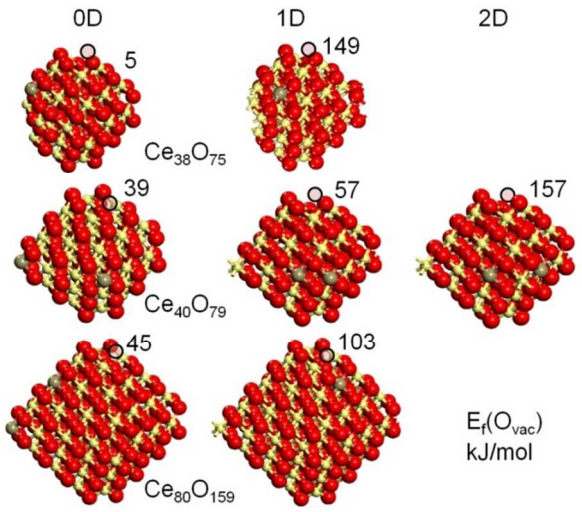

Fig. 3 Oxygen defective Ce_nO_{2n-1} NPs for the 0D, 1D and 2D structures displayed in Fig. 1, which contain one per NP most easily formed O_{2c} vacancy at the top O_4 sites with the corresponding oxygen vacancy formation energies $E_f(O_{vac})$ [kJ/mol] calculated vs. ½ O_2 triplet state energy. Ce^{4+} cations – light beige spheres, Ce^{3+} cations – dark beige spheres, O^{2-} anions – red spheres, position of O_{vac} – black circles. As a result of the adopted orientation, only one Ce^{3+} cation is visible for 0D, 1D $Ce_{38}O_{75}$ and 1D $Ce_{80}O_{159}$.

For 1D $Ce_{40}O_{79}$, we also inspected the stability of the Ce^{3+} configuration with one 4f electron at the connected corner Ce atom and the other at the free corner Ce atom. This configuration is less stable (by 45 kJ/mol, Fig. S2) than the computed most stable configuration ($E_f(O_{vac})$ = 57 kJ/mol), indicating that the connected corner Ce atom may not be easily reduced. This increment is consistent with $\left|\varepsilon_{4f}^{edge} - \varepsilon_{4f}^{corner\,1}\right|$ = 0.37 eV in the pristine 1D $Ce_{40}O_{80}$ structure. For 2D $Ce_{40}O_{79}$, the Ce^{3+} configuration with the 4f electrons localized separately at the connected corner Ce atoms ($\varepsilon_{4f}^{corner\,1} = \varepsilon_{4f}^{corner\,2}$ = -3.85 eV in the pristine 2D $Ce_{40}O_{80}$ structure) was found to be somewhat less stable (by 23 kJ/mol, Fig. S2) than the computed most stable configuration. This increment is smaller than that obtained for 1D $Ce_{40}O_{79}$. It is consistent with $\left|\varepsilon_{4f}^{edge} - \varepsilon_{4f}^{corner\,1}\right| + \left|\varepsilon_{4f}^{edge} - \varepsilon_{4f}^{corner\,2}\right|$ = 0.06 eV in 2D $Ce_{40}O_{80}$ being smaller than $\left|\varepsilon_{4f}^{edge} - \varepsilon_{4f}^{corner\,1}\right|$ = 0.37 eV in 1D $Ce_{40}O_{80}$. These results show that the electronic structure properties of the PDOS on the total 4f levels of the pristine structure influence directly the energy difference between different Ce^{3+} configurations. W_{4f} for 2D $Ce_{40}O_{80}$ is smaller than that for 1D $Ce_{40}O_{80}$. Correspondingly, the energy difference between different Ce^{3+} configurations spans a smaller energy range for 2D $Ce_{40}O_{80}$ as compared to 1D $Ce_{40}O_{80}$.

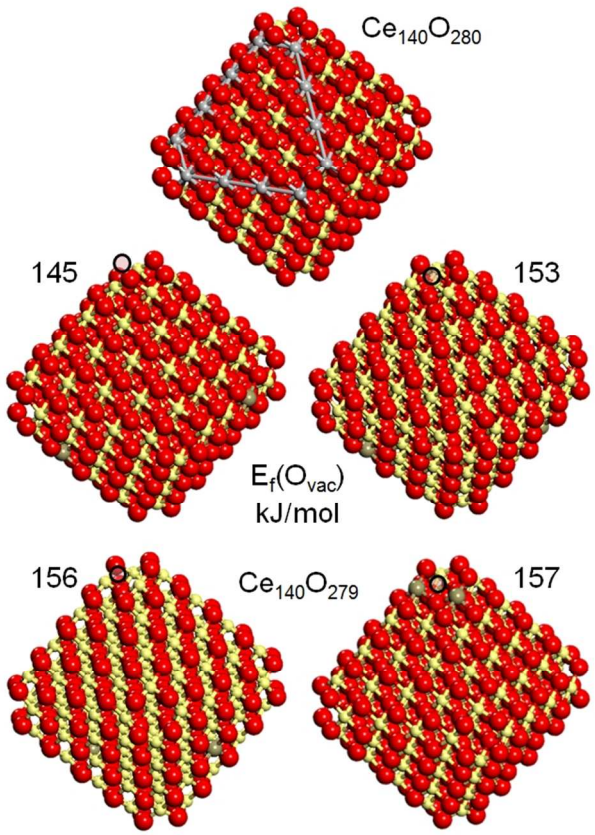

Fig. 4 Sketches of a stoichiometric ceria $Ce_{140}O_{280}$ NP and oxygen defective $Ce_{140}O_{279}$ NPs with an O_{2c} vacancy at the top O_4 site with the corresponding oxygen vacancy formation energies $E_f(O_{vac})$ [kJ/mol] calculated vs. ½ O_2 triplet state energy for various Ce^{3+} configurations. Ce^{4+} cations – light beige spheres, Ce^{3+} cations – dark beige spheres, O^{2-} anions – red spheres, position of O_{vac} – black circles, edges of one {111} facet – silver spheres.

In $Ce_{80}O_{159}$ one 4f electron was localized at the available corner Ce atom ($\varepsilon_{4f}^{corner\,1}$ = -4.24 eV in $Ce_{80}O_{160}$) and the other 4f electron was localized at a nearby edge Ce atom (ε_{4f}^{edge} = -3.90 eV in $Ce_{80}O_{160}$). In 1D $Ce_{80}O_{159}$ one 4f electron was localized at a facet Ce site in the proximity of the vacancy (ε_{4f}^{facet} = -3.84 eV in 1D

$Ce_{80}O_{160}$) and the other 4f electron was localized at an edge Ce atom (ε_{4f}^{edge} = -3.90 eV in 1D $Ce_{80}O_{160}$). Based on the $\varepsilon_{2p}^{O_{2c}}$ and W_{4f} values, larger $E_f(O_{vac})$ values are expected for 1D $Ce_{80}O_{160}$ as compared to $Ce_{80}O_{160}$. However, a somewhat smaller $E_f(O_{vac})$ increment (58 kJ/mol) between 0D $Ce_{80}O_{160}$ and 1D $Ce_{80}O_{160}$ than the expected one is found. This result may be related to the relaxation energy contribution to $E_f(O_{vac})$ for 1D $Ce_{80}O_{160}$. A significant energy gain is expected for localization at the facet site in the proximity of the vacancy. This is because the total Ce-O bond expansion of the seven Ce-O bonds of the facet Ce atom associated with the localization of the 4f electron at this site is particularly pronounced (90 pm). The creation of the O vacancy for 0D $Ce_{38}O_{76}$ is nearly energy-neutral (5 kJ/mol), but is significantly more difficult (149 kJ/mol) in 1D $Ce_{38}O_{76}$.

Overall, Fig. 3 shows that the self-assembly has direct consequences on $E_f(O_{vac})$. For each building block size, larger $E_f(O_{vac})$ values are computed for the 1D or 2D arrays with respect to the 0D building blocks. These changes in $E_f(O_{vac})$ are controlled by the effect of the creation of the Ce-O_4 and Ce_4-O_4 contacts on the electronic structure (Fig. 2 and Table 1), which corresponds to a stabilization of $\varepsilon_{2p}^{O_{2c}}$ as well as a decrease of W_{4f}. The NPs or nanoarrays with corner Ce atoms or a Ce-terminated facet ($Ce_{38}O_{76}$, $Ce_{40}O_{80}$, 1D $Ce_{40}O_{80}$ and 0D $Ce_{80}O_{160}$), which have larger W_{4f} values and higher $\varepsilon_{2p}^{O_{2c}}$ energies, have smaller $E_f(O_{vac})$ as compared to the nanoarrays with no corner Ce atoms or a Ce-terminated facet (1D $Ce_{38}O_{76}$, 1D $Ce_{80}O_{160}$ and 2D $Ce_{40}O_{80}$), which instead have smaller W_{4f} values and lower $\varepsilon_{2p}^{O_{2c}}$ energies. A rather low $E_f(O_{vac})$ value was reported for $Ce_{40}O_{80}$´ (77 kJ/mol, Table 1),[6,7] which also exposes two corner Ce atoms. Overall we find a similar $E_f(O_{vac})$ ordering as for W_{4f}, implying that $E_f(O_{vac})$ and W_{4f} are interrelated.

To better understand the $E_f(O_{vac})$ changes induced by the NP self-assembly we also computed the energy for removal of an O_{2c} atom from the O_4 site of the $Ce_{140}O_{280}$ NP. The two excess Ce^{3+} cations were localized on edge Ce sites (Fig. 4). A small $E_f(O_{vac})$ difference (12 kJ/mol at most) is found between the various Ce^{3+} configurations. This result is similar to that discussed above for 2D $Ce_{40}O_{80}$ and depends on the narrow 4f PDOS bandwidth (W_{4f} ~ 0.1 eV). A second important observation is that the lowest $E_f(O_{vac})$ value for $Ce_{140}O_{280}$ is similar though somewhat smaller than the lowest $E_f(O_{vac})$ value for 2D $Ce_{40}O_{80}$. As already mentioned, 2D $Ce_{40}O_{80}$ and $Ce_{140}O_{280}$ have similar electronic structures, with the most significant difference being a small shift (0.15 eV) towards lower energies for $\varepsilon_{2p}^{O_{2c}}$, which may explain the slightly larger $E_f(O_{vac})$ value computed for 2D $Ce_{40}O_{80}$. This is a further evidence for the stringent resemblance between 2D $Ce_{40}O_{80}$ and $Ce_{140}O_{280}$.

$\varepsilon_{2p}^{O_{2c}}$ may differ from the 2p highest occupied molecular orbital (HOMO) energy, e.g., the HOMO of Ce_nO_{2n} (n=38, 40, 80) and 1D $Ce_{40}O_{80}$ in Fig. 2 is given by the 2p levels of the O_4 site, which forms the contact (cfr. highest energy peak in the blue and red filled PDOS). Moreover, several Ce atoms usually contribute to the 4f lowest unoccupied molecular orbital (LUMO), except for structures with corner Ce atoms. Here the LUMO essentially corresponds to one of the seven 4f levels of the corner Ce atom. Despite these differences, we find that the modulations of $E_f(O_{vac})$ can be nicely correlated with concomitant variations of the O 2p HOMO and Ce 4f LUMO energy difference, Δε in Table 1. Thus, Δε can also be considered as a practical descriptor of the facility to form O vacancies in CeO_2 nanostructures.

Comparison between PW91+4 and HSE06 approaches.

To corroborate the PW91+4 results, we evaluated $E_f(O_{vac})$ using the HSE06 functional[26,27] for 0D, 1D, and 2D $Ce_{40}O_{80}$, $Ce_{40}O_{80}$´. To generalize our comparison, we also consider the HSE06 $E_f(O_{vac})$ data for regular[30,31] and three (I - III) vicinal stepped $CeO_2(111)$ surface models,[31] and for $Ce_{21}O_{42}$.[6,7] For the extended systems, we considered O atoms with different coordination numbers. In particular, we computed $E_f(O_{vac})$ for removal of: a subsurface four-coordinated oxygen atom, O_{4c}, from a regular $CeO_2(111)$ model; a three-coordinated oxygen atom, O_{3c}, from the step of a $CeO_2(111)$ model with step type I; a two-coordinated oxygen atom, O_{2c}, from the step of $CeO_2(111)$ models with step types II and III (Fig. S3). These O_{vac} positions and associated Ce^{3+} configurations correspond to the most stable ones for the models employed.[31]

As shown in Fig. 5, the $E_f(O_{vac})$ values calculated with the PW91+4 approach correlate remarkably well (R^2=0.99) with the values obtained with the HSE06 hybrid functional. The difference between the $E_f(O_{vac})$ values predicted by the two approaches is somewhat dependent on the system. For $Ce_{21}O_{42}$ $E_f(O_{vac})^{HSE06}$ is 37 kJ/mol larger than $E_f(O_{vac})^{PW91+4}$ (Table 2). This difference is somewhat larger (~60–70 kJ/mol) for $Ce_{40}O_{80}$, $Ce_{40}O_{80}$´ and 1D $Ce_{40}O_{80}$. A smaller deviation (~20 kJ/mol) is computed for 2D $Ce_{40}O_{80}$. The HSE06 and PW91+4 schemes predict almost the same energy for O_{vac} formation for the regular and the three vicinal $CeO_2(111)$ surfaces. This correlation validates the reliability of the PW91+4 $E_f(O_{vac})$ trends for the NPs and nanoarchitectures with different size and dimensionality discussed within the present work.

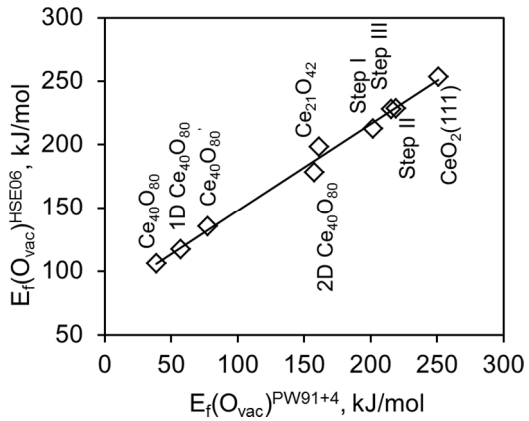

Fig. 5 Correlation between the oxygen vacancy formation energy computed with the HSE06 and PW91+4 functionals, $E_f(O_{vac})^{HSE06}$ and $E_f(O_{vac})^{PW91+4}$, for $Ce_{21}O_{42}$, $Ce_{40}O_{80}$´ and $Ce_{40}O_{80}$ NPs, 1D, and 2D $Ce_{40}O_{80}$ nanoarchitectures, regular and three vicinal $CeO_2(111)$ surfaces. The fitted correlation (in kJ/mol): $E_f(O_{vac})^{HSE06}$ = 79 + 0.68 $E_f(O_{vac})^{PW91+4}$, R^2 = 0.99.

The correlation is very useful as it can provide estimates with an acceptable uncertainty for $E_f(O_{vac})$ for systems that have too many atoms to be treated at the more expensive HSE06 level of theory. The HSE06 estimates for 0D, 1D $Ce_{80}O_{160}$ and $Ce_{140}O_{280}$ from the linear correlation in Fig. 5 are 110, 150 and 178 kJ/mol, respectively. The $E_f(O_{vac})^{HSE06}$ values for $Ce_{140}O_{280}$ and 2D $Ce_{40}O_{80}$ (178 kJ/mol, Table 2) although are increased with respect to the other nanostructures, still remain smaller by 75 kJ/mol than the value for the regular $CeO_2(111)$ surface. These values are also smaller by 35 kJ/mol than the $E_f(O_{vac})^{HSE06}$ value obtained for the vicinal $CeO_2(111)$ surface with step type I (213 kJ/mol, Table 2). Thus, the O_{vac} formation is found to be greatly facilitated in Ce_nO_{2n} nanostructures compared with regular and vicinal $CeO_2(111)$ surfaces. This facility to form O vacancies in nanostructured CeO_2 is instrumental to understand the remarkable activity documented for these systems.[4,5]

Table 2. Comparison of lowest O atom vacancy formation energy, ($E_f(O_{vac})$), and the O 2p HOMO and Ce 4f LUMO energy difference, ($\Delta\varepsilon$), for various CeO_2 systems, calculated with the PW91+4 and HSE06 approaches.

Model	$E_f(O_{vac})$, kJ/mol		$\Delta\varepsilon$, eV	
	PW91+4	HSE06	PW91+4	HSE06
CeO_2(111) regular[a]	251[d]	253[b,c,d]	2.01	3.17
Step I[a]	201[d]	213[d]	2.12	3.06
Step II[a,e]	216	228	1.77	2.77
Step III[a]	219[d]	228[d]	2.05	3.49
0D $Ce_{21}O_{42}$	161	198	1.91	3.19
0D $Ce_{40}O_{80}$´	77	135	1.49	2.83
0D $Ce_{40}O_{80}$	39	105	0.97	2.22
1D $Ce_{40}O_{80}$	57	117	1.15	2.46
2D $Ce_{40}O_{80}$	157	178	1.76	3.05

[a]See Fig. S2. [b]The PW91+4 $E_f(O_{vac})$ value computed for a $p(3 \times 4)$ CeO_2(111) surface unit cell with three CeO_2 layers employing the experimental/optimized (541/549 pm) lattice constant is 245/217 kJ/mol[30]. [c]A lower $E_f(O_{vac})$ value (218 kJ/mol) was reported8 for a $p(4 \times 4)$ CeO_2(111) surface unit cell, which corresponds to a defect concentration Θ = 1/16 monolayer of O atoms. [d]The difference with respect to the values in ref. 31 is due to the lack of inclusion in this work of the aspheric gradient correction within the PAW sphere. [e]The position of one Ce^{3+} cation is different with respect to ref. 31.

Conclusions

To summarize, the present work provides a rationalization based on the electronic structure analysis for the variations of $E_f(O_{vac})$ values reported as function of the size and dimensionality for the Ce_nO_{2n} (n=38, 40, 80) NPs and their self-assemblies. The PW91+4 $E_f(O_{vac})$ trends have been verified based on HSE06 single-point energy calculations at PW91+4 optimized geometries for selected structures. This study shows that the presence of certain structural features can appreciably affect the global electronic structure, in particular with regards to the shape and bandwidth of the unoccupied DOS projected onto the Ce 4f levels, which ultimately impact on the $E_f(O_{vac})$ values. Our work identifies the corner Ce atoms as a structural motif essential for a significant reduction of $E_f(O_{vac})$. The remarkable electronic similarity between 1D $Ce_{80}O_{160}$, 2D $Ce_{40}O_{80}$ and $Ce_{140}O_{280}$ may have important implications. For instance, in theoretical studies, one may approach bigger NPs through computationally less demanding assembly of much smaller NPs.

We emphasize the model character of the present work, which is a first step in electronic structure investigations of ceria nanoarchitectures. Based on our findings presence and disappearance of corner Ce atoms in ceria nanoarchitectures is predicted to significantly affect propensity to form O vacancies. The presence of such sites in ceria based catalysts will significantly affect their red-ox properties. Moreover another pivotal structural motif, the O_4 unit on small {100} facets, present in the studied nanoarrays, has been recently identified experimentally as an abundant element in ceria based nanomaterials.[11] Thus, the outcome of this study appears to be relevant also for nanoarchitectures that are formed from larger building blocks or even for nanostructured ceria without clear regularity.

Acknowledgements

Financial support has been provided by the European Community (FP7-NMP.2012.1.1-1 project ChipCAT, Ref. Nº310191), the Spanish MINECO (CTQ2012-34969, FIS2012-37549-C05-02, RYC-2011-09582) and the Generalitat de Catalunya (2014SGR97, 2014SGR301, XRQTC). SMK thanks the Spanish Ministerio de Educación for a pre-doctoral FPU grant AP2009-3379. MAS and KHL acknowledge funding from MOE/ AcRF RG73/10. This work is a part of the COST Action CM1104 "Reducible oxide chemistry, structure and functions". Computer resources, technical expertise and assistance provided by the Red Española de Supercomputación are gratefully acknowledged.

Notes and references

[a] School of Chemical and Biomedical Engineering, Nanyang Technological University, Singapore 639798.

[b] Departament de Química Física and Institut de Quimica Teòrica i Computacional (IQTCUB), Universitat de Barcelona, 08028 Barcelona, Spain.

[c] Singapore Institute of Technology, 10 Dover Drive, Singapore 138683.

[d] CSIC - Consejo Superior de Investigaciones Científicas, ICN2 Building, Campus UAB, 08193 Bellaterra, Spain.

[e] ICN2 - Institut Català de Nanociència i Nanotecnologia, ICN2 Building, Campus UAB, 08193 Bellaterra, Spain.

[f] Institució Catalana de Recerca i Estudis Avançats (ICREA), 08010 Barcelona, Spain.

† Electronic Supplementary Information (ESI) available: Figure for $Ce_{40}O_{80}$ and $Ce_{40}O_{80}$´. $E_f(O_{vac})$ results for additional Ce^{3+} configurations for the Ce_nO_{2n} (n=38, 40, 80) NPs and their self-assemblies. $E_f(O_{vac})$ results for regular and three (I - III) vicinal stepped CeO_2(111) surface models. Cartesian Coordinates for the Ce_nO_{2n} (n=38, 40, 80, 140) NPs. See DOI: 10.1039/b000000x/

1 C. Sun, H. Hong Li and L. Chen, *Energy Environ. Sci.*, 2012, **5**, 8475-8505.
2 Catalysis by Ceria and Related Materials, Catalytic Science Series, Vol. 12, ed. A. Trovarelli and P. Fornasiero, Imperial College Press: London, U. K., 2nd edn., 2013.
3 S. T. Bromley, I. de P. R. Moreira, K. M. Neyman and F. Illas, *Chem. Soc. Rev.*, 2009, **38**, 2657-2670.
4 S. Carrettin, P. Concepcion, A. Corma, J. M. L. Nieto, and V. F. Puntes, *Angew. Chem. Int. Ed.*, 2004, **43**, 2538-2540.
5 J. Guzman, S. Carrettin and A. Corma, *J. Am. Chem. Soc.*, 2005, **127**, 3286-3287.
6 A. Migani, G. N. Vayssilov, S. T. Bromley, F. Illas and K. M. Neyman, *Chem. Commun.*, 2010, **46**, 5936-5938.
7 A. Migani, G. N. Vayssilov, S. T. Bromley, F. Illas and K. M. Neyman, *J. Mater. Chem.*, 2010, **20**, 10535-10546.
8 J. Paier, C. Penschke and J. Sauer, *Chem. Rev.*, 2013, **113**, 3949-3985.
9 G. N. Vayssilov, Y. Lykhach, A. Migani, T. Staudt, G. P. Petrova, N. Tsud, T. Skála, A. Bruix, F. Illas, K. C. Prince, V. Matolin, K. M. Neyman and J. Libuda, *Nature Mater.*, 2011, **10**, 310-315.
10 Q. Fu, H. Saltsburg and M. Flytzani-Stephanopoulos, *Science*, 2003, **301**, 935-938.
11 A. Bruix, Y. Lykhach, I. Matolínová, A. Neitzel, T. Skála, N. Tsud, M. Vorokhta, V. Stetsovych, K. Ševčíková, J. Mysliveček, R. Fiala, M. Václavů, K. C. Prince, S. Bruyère, V. Potin, F. Illas, V. Matolín, J. Libuda and K. M. Neyman, *Angew. Chemie Int. Ed.*, 2014, DOI:10.1002/anie.201402432.

12 H.-X. Mai, L.-D. Sun, Y.-W. Zhang, R. Si, W. Feng, H.-P. Zhang, H.-C. Liu and C.-H. Yan, *J. Phys. Chem. B*, 2005, **109**, 24380-24385.
13 S. Yang, L and Gao, *J. Am. Chem. Soc*., 2006, **128**, 9330-9331.
14 N. Du, H. Zhang, B. Chen, X. Ma and D. Yang, *J. Phys. Chem. C*, 2007, **111**, 12677-12680.
15 X. Liu, K. Zhou, L. Wang, B. Wang and Y. Li, *J. Am. Chem. Soc.*, 2009, **131**, 3140-3141.
16 T. X. T. Sayle, M. Cantoni, U. M. Bhatta, P. S. Parker, S. R. Hall, G. Möbus, M. Molinari, D. Reid, S. Seal and D. C. Sayle, *Chem. Mater.*, 2012, **24**, 1811-1821.
17 Z. Tang and N. A. Kotov, *Adv. Mater.*, 2005, **17**, 951-962.
18 F. Viñes, F. Illas, K. M. Neyman, *Angew. Chem. Int. Ed*., 2007, **46**, 7094–7097.
19 J. P. Perdew, J. A. Chevary, S. H. Vosko, K. A. Jackson, M. R. Pederson, D. J. Singh and C. Fiolhais, *Phys. Rev. B*, 1992, **46**, 6671-6687.
20 J. P. Perdew, J. A. Chevary, S. H. Vosko, K. A. Jackson, M. R. Pederson, D. J. Singh and C. Fiolhais, *Phys. Rev. B*, 1993, **48**, 4978.
21 J. P. Perdew and Y. Wang, *Phys. Rev. B*, 1992, **45**, 13244.
22 C. Loschen, J. Carrasco, K. M. Neyman, F. Illas, *Phys. Rev. B*, 2007, **75**, 035115; *ibid*, 2011, **84**, 199906(E).
23 V. I. Anisimov, F. Aryasetiawan, and A. I. Lichtenstein, *J. Phys.: Condens. Matter*, 1997, **9**, 767–808.
24 S. L. Dudarev, G. A. Botton, S. Y. Savrasov, C. J. Humphreys and A. P. Sutton, *Phys. Rev. B*, 1998, **57**, 1505.
25 A. Migani, K. M. Neyman and S. T. Bromley, *Chem. Commun.*, 2012, **48**, 4199-4201.
26 J. Heyd, G. E. Scuseria and M. Ernzerhof, *J. Chem. Phys.*, 2003, **118**, 8207.
27 J. Heyd, G. E. Scuseria and M. Ernzerhof, *J. Chem. Phys.*, 2006, **124**, 219906.
28 J. Paier, M. Marsman, K. Hummer, G. Kresse, I. C. Gerber and J. G. Ángyán, *J. Chem. Phys.*, 2006, **124**, 154709.
29 J. Paier, M. Marsman, K. Hummer, G. Kresse, I. C. Gerber and J. G. Ángyán, *J. Chem. Phys.*, 2006, **125**, 249901.
30 A. Bruix, A. Migani, G. N. Vayssilov, K. M. Neyman, J. Libuda and F Illas, *Phys. Chem. Chem. Phys.*, 2011, **13**, 11384-11392.
31 S. M. Kozlov and K. M. Neyman, *Phys. Chem. Chem. Phys*., 2014, **16**, 7823-7829.
32 G. Kresse and J. Hafner, *Phys. Rev. B*, **1993**, **47**, 558-561.
33 G. Kresse and J. Furthmüller, *Phys. Rev. B*, 1996, **54**, 11169-11186.
34 M. V. Ganduglia-Pirovano, J. L. F. Da Silva and J. Sauer, *Phys. Rev. Lett.*, 2009, **102**, 026101.
35 J. L. F. Da Silva, M. V. Ganduglia-Pirovano, J. Sauer, V. Bayer and G. Kresse, *Phys. Rev. B*, 2007, **75**, 045121.
36 G. Kresse and D. Joubert, *Phys. Rev. B*, 1999, **59**, 1758-1775.
37 R. F. W. Bader, Atoms in Molecules, Oxford University Press: Oxford, U. K., 1990.
38 D. J. Mowbray, A. Migani, G. Walther, D. M. Cardamone and A. Rubio, *J. Phys. Chem. Lett.*, 2013, **4**, 3006-3012.
39 S. J. Duclos, Y. K. Vohra, A. L. Ruoff, A. Jayaraman, and G. P. Espinosa, *Phys. Rev. B*, 1988, **38**, 7755-7758.
40 L. Gerward and J. S. Olsen, *Powder Diffr.*, 1993, **8**, 127-129.
41 A. S. Barnard; A. I. Kirkland, *Chem. Mater.*, 2008, **20**, 5460-5463.
42 Z. L.Wang and X. D. Feng, *J. Phys. Chem. B*, 2003, **107**, 13563-13566.
43 T. X. T. Sayle, S. C. Parker and D. C. Sayle, *Chem. Commun,*. 2004, 2438-2439.
44 C. Loschen, S. T. Bromley, K. M. Neyman, and F.Illas, *J. Phys. Chem. C*, 2007, **111**, 10142-10145.
45 C. Loschen, A. Migani, S. T. Bromley, F. Illas and K. M. Neyman, *Phys. Chem. Chem. Phys.*, 2008, **10,** 5730-5738.
46 The $Ce_{38}O_{76}$ structure is merely a sub-system of the $Ce_{40}O_{80}$ NP obtained without an attempt to approach the lowest-energy NP for this size. It has been included to account for the interaction between Ce and O terminated facets.
47 A. Migani, C. Loschen, F. Illas, and K. M. Neyman, *Chem. Phys. Lett.*, 2008, **465**, 106-109.
48 $Ce_{140}O_{280}$ is derived from the perfect under-stoichiometric octahedral $Ce_{146}O_{280}$ bulk cut by removal of the excess six Ce corner atoms, which results in six O_4 sites and no corner Ce atoms.